Advanced Thermoelectric Power Generation System for Low Enriched Uranium Fuel Reactors

Troy M. Howe[1], Steven D. Howe[2] and Jack R. Miller[3]
Howe Industries, LLC, Scottsdale, AZ, 85260

and

Nicholas S. Campbell[4]
The Hypershield Partnership, LLC, Longmont, CO, 80501

Interplanetary space exploration probes provide a multitude of scientific knowledge about our solar system. In the past, these probes have been powered by radioisotope fuel sources, with the primary radioisotope being plutonium. Due to plutonium's scarcity, identifying alternative nuclear-powered energy sources is crucial to enabling future space probe missions. Many of the current alternative power sources are mass intensive, require a tightly regulated fuel known as highly enriched uranium (HEU), and require complex moving systems to produce power. Howe Industries LLC proposes a novel method of drastically increasing current thermoelectric generator (TEG) power production to provide an improved solution for deep-space power systems. Through testing of various materials and funding from NASA's Innovative Advanced Concepts (NIAC) Program, Howe Industries has experimentally shown the potential for massive breakthroughs in thermoelectric generator efficiencies that could compete with current power production alternatives. These advanced thermoelectric generators (ATEGs) can be applied to deep space technologies in conjunction with a low enriched uranium (LEU) reactor which can be privately owned by companies in the United States. With the use of this highly efficient solid-state energy system, deep space missions and high magnitude power production will become more feasible for future space exploration. This paper will outline the method Howe Industries LLC proposes to increase the efficiency of current thermoelectric technologies for power production.

Nomenclature

a	=	cylinder diameter
ϵ	=	emissivity
η	=	efficiency
F_{self}	=	view factor
I_{sol}	=	solar constant
κ	=	thermal conductivity
n	=	n-type thermoelectric
n_{fins}	=	number of fins
p	=	p-type semiconductor
$Q_{th,w}$	=	heat load
S	=	Seebeck coefficient
σ	=	electric conductivity
T	=	temperature
T_c	=	cold junction temperature
T_h	=	hot junction temperature
zT	=	thermoelectric material figure of merit
$Z\bar{T}$	=	average figure of merit

[1] President, 1435 E. University Dr. Ste C-108, Tempe, AZ 85281
[2] Head of Research, 1435 E. University Dr. Ste C-108, Tempe, AZ 85281
[3] Research and Development Engineer, 1435 E. University Dr. Ste C-108, Tempe, AZ 85281
[4] Founder and Chief Technical Partner, 847 Sumner St., Longmont, CO 80501

I. Introduction

THE exploration and development of space in the modern age is quickly reaching an unprecedented level of commercial involvement. Mega-constellations, lunar payload delivery services, and private launch vehicles are some examples of innovations in the space ecosystem that have been driving future development in space exploration. One niche in space exploration that remains beyond the reach of commercial entities, is deep space exploration due to prohibitive costs that only government programs could justify. Howe Industries, with support from a NASA Innovative and Advanced Concepts (NIAC) investigation, has laid out the preliminary design for a nuclear-powered, deep space probe, which can be owned and operated by private industry. This design, called the Swarm Probe Enabled ATEG Reactor (SPEAR), utilizes nuclear electric propulsion (NEP) and advanced thermoelectric generators (ATEGs) to deliver payloads into deep space while reducing costs. A demonstration mission to the Jovian moon, Europa, was created to highlight the capabilities and advantages of the SPEAR probe.

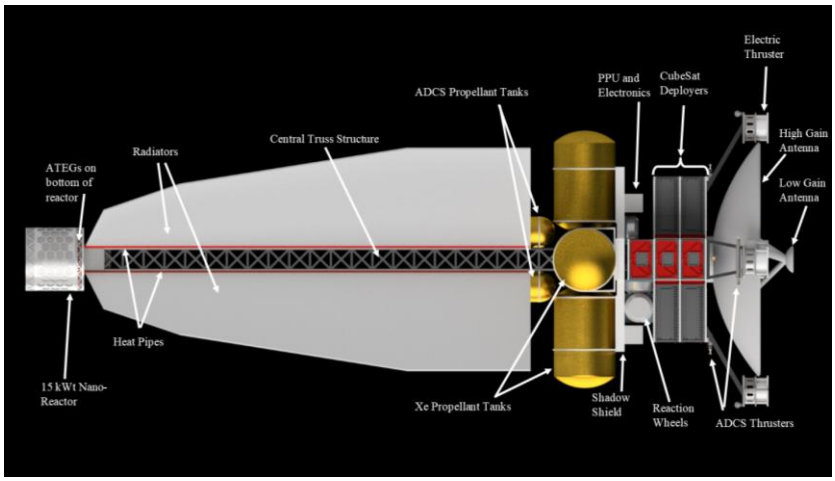

Figure 1. Artist rendition of SPEAR probe enabling exploration of Europa and deep space with a swarm of CubeSats. The nano-reactor providing and power conversion system rest on the primary trust structure away from the payload to decrease the total ionizing dose experienced by the payload and flight systems.

The SPEAR spacecraft has been designed to minimize its mass, allowing it to be launched on most US-based, small satellite launch vehicles. This was done to minimize launch costs and maximize the range of launch vehicles capable of transporting SPEAR to orbit. Figure 1 shows an artist rendering of the SPEAR spacecraft, with a payload of CubeSats, to explore the Jovian moon of Europa. A 15kW low enriched uranium nano-reactor with ATEGS enabling 3kW of power generation resides on the forward end of SPEAR. While there is approximately 3 meters of separation from the reactor to the payload, large radiators, matching the contours of a Minotaur IV fairing, have been added to reject the 12 kW of thermal power from the reactor. For the demonstration mission, a configuration of 10 CubeSats, weighing approximately 7kg each, are used to analyze the content of ejecta from Europa's plumes, and SPEAR's large parabolic antenna enables deep space communication with Earth. With an estimated mass of just over 1500 kg, SPEAR is a highly capable probe that enables affordable deep space exploration.

II. Advanced Thermoelectric Generators

The cornerstone of SPEAR's success lies within the advanced thermoelectric generators. These generators enable the >20% conversion efficiency needed to achieve 3kW of electrical power for SPEAR's electric thrusters. With this revolutionary technology, SPEAR will produce more power than any previous deep space probe, without the need for large solar panels or radioisotope thermoelectric generator (RTG) power sources. Howe Industries has investigated the validity of this system, and its potential to revolutionize thermoelectric generator (TEG) technologies beyond levels thought to be infeasible.

The principals behind thermoelectric technologies are well known, and many strides have been taken to increase thermoelectric performance. However, many have fallen short of the technical breakthroughs required to make TEG powered nuclear electric propulsion (NEP) systems viable. Thermoelectric materials are characterized by their figure of merit, which is defined by the following equation:

$$zT = \frac{S^2 T}{\frac{\kappa}{\sigma}} \tag{1}$$

In this equation zT is the figure of merit, S is the Seebeck coefficient, T is the temperature, κ, is the material's thermal conductivity, and σ is the material's electrical conductivity. A larger figure of merit results in a higher performing

thermoelectric material. Equation 1 is applicable to a single material, but TEGs consist of both p-type and n-type thermoelectric materials, and therefore the average figure of merit for such a thermoelectric generator is expressed with the following equation:

$$Z\bar{T} = \frac{\left(S_p - S_n\right)^2 \bar{T}}{\left(\left(\frac{\kappa_p}{\sigma_p}\right)^{\frac{1}{2}} + \left(\frac{\kappa_n}{\sigma_n}\right)^{\frac{1}{2}}\right)^2} \tag{2}$$

In this case $\bar{T}$ is the average temperature between the hot and cold junctions, S_p, S_n, κ_p, κ_n, σ_p, σ_n represent the Seebeck coefficient, thermal conductivity, and electrical conductivity of the p-type and n-type semiconductors, respectively. It is obvious from these equations that increasing the electrical conductivity, average temperature, Seebeck coefficient, and decreasing the thermal conductivity are all viable methods to increase the average figure of merit. This figure of merit directly translates to the efficiency of the thermoelectric generator, described in the following equation:

$$\eta = \frac{\Delta T}{T_h} \frac{\sqrt{1 + Z\bar{T}} - 1}{\sqrt{1 + Z\bar{T}} + \frac{T_c}{T_h}} \tag{3}$$

Where η is the overall conversion efficiency, T_h is the hot junction temperature, and T_c is the cold junction temperature of the TEG. The first portion of this equation is the Carnot Efficiency, which is the theoretical maximum efficiency that can be achieved. As $Z\bar{T}$ approaches infinity, the conversion efficiency approaches the Carnot limit.

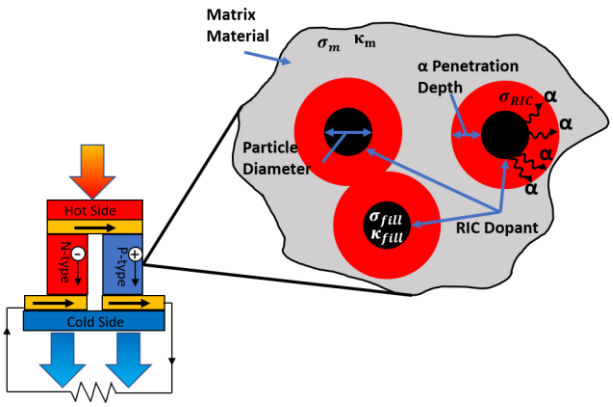

Figure 2. This figure demonstrates the mechanisms behind the ATEGs. The RIC dopant is used within the material matrix to create localized areas of increased conductivity. With enough dopant the bulk conductivity of the thermoelectric material will change, increasing the ATEG's figure of merit and conductivity.

While increasing the temperature gradient between the hot and cold side is a simple method to increase the efficiency, this is not an effective method to increase efficiency, as many systems may not be capable of maintaining high temperature gradient between the hot and cold sides. As mentioned previously, this figure of merit is dependent on the material properties, which have proven difficult to change. Typical thermoelectric generators in RTGs can reach 6.3% efficiencies[1]. Dynamic cycles may achieve efficiencies as high as 30%[1] but require working fluids and moving machinery.

Howe Industries has investigated the possibility of increasing different thermoelectric materials' figure of merit to outpace the performance of current deep space and terrestrial solid-state power generation systems. This is accomplished through a phenomenon known as radiation induced conductivity (RIC). A graphic depicting this phenomenon is visible in Figure 2. This unique process involves ionizing radiation that causes atoms in a target material to ionize and free its electrons, which increases the electrical conductivity of the material. These electrons eventually return to their host (target) nucleus, returning the electrical conductivity of the material.. This process is dependent on supplying a constant source of ionizing radiation to maintain a constant state of elevated electrical conductivity. Utilizing this phenomena, the electrical conductivity of the ATEG can be changed to drastically increase the figure of merit and therefore its achievable efficiency.

The degree of conductivity changes is under investigation, as relevant data significant information over a range of materials is not available. However, an experiment at Oak Ridge National Laboratory (ONRL) by Ref 2 observed an increase of 400x in the electrical conductivity of alumina when exposed to ionizing radiation, at temperatures within

our operating range. Another experiment on ceramic materials observed over 10,000 times increase in electrical conductivity in a UV grade sapphire sample inside a reactor core[3]. As stated, the most effective method to increase the efficiency of these TEGs, is to change the electrical conductivity of the sample. Modification of the Seebeck coefficient and thermal conductivity due to radiation exposure has also shown positive results, Ref. 4 and 5.

A continuous source of ionizing radiation must be present for this phenomenon to occur; with a nano-reactor available on SPEAR, this ionizing radiation is ever present. Other sources may include radioisotope particles that naturally produce ionizing radiation, such as ^{241}Am and ^{238}Pu, as well as (n, α) materials that produce alpha particles when they interact with neutrons.

These RIC dopants will be used to effectively change the electrical conductivity of thermoelectric materials. Different RIC dopants will have various effects on the electrical conductivity of the sample. This is mostly due to the energy of the ionizing radiation emitted from the dopant. The particle size, vol% infill, and ionizing particle energy all determine the total volume of the thermoelectric material under RIC influence. The significant advantage of (n, α) dopant is their availability compared to radioisotope sources. However, radioisotope sources can operate independently of a neutron flux and could be applied to heritage multi-mission radioisotope thermoelectric generators (MMRTG).

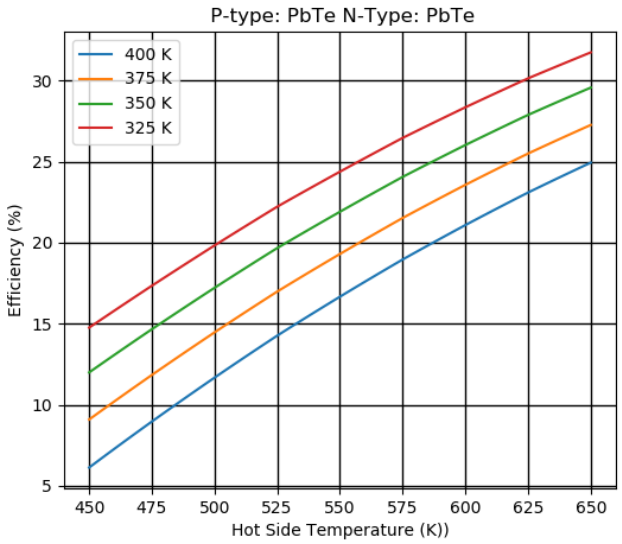

Figure 3. Models show large increases in tradiational thermoelectric generators with modest RIC effects. In this example SPEAR would maintain an efficiency greater than 25% at its operational temperature gradient. This p-type and n-type pair would traditionally have ~6% efficiency at this temperature gradient.

Initial models in this Phase I study have shown only small RIC effects are necessary to drastically increase the efficiency of these thermoelectric generators. Such effects on efficiency are visible in Figure 3, with PbTe as the p-type and n-type foot and an (n, α) dopant; this pair of semiconductors would produce a theoretical efficiency of ~6% without the presence of an RIC dopant, but can reach over 25% efficiencies, at the operational temperatures of SPEAR, with the RIC dopant applied. Table 1 shows the power, and specific power, associated with a 25% efficient ATEG power conversion system applied to heritage nuclear power systems. Also, it is expected the ATEG power conversion system will have an equivalent mass to the traditional TEG conversion system. In Table 1, the advanced sterling radioisotope generator (ASRG) maintains a slightly higher efficiency than the ATEG system, but one must consider the advantages of a power conversion system that involves no moving parts or working fluids.

Table 1. Heritage space-based nuclear power systems utilizing radioisotope decay as a heat source. ATEG conversion system values are highlighted. Significant increases in power output, as well as specific power are visible. Values provided by Ref. 1 and 6.

	GPHS-RTG	MMRTG	ASRG
Heat Input, Wt	4500	2000	500
Electric output, We	285	125	150
Electric output w/ATEGs, We	1125	500	125
Total system weight, kg	56	44.2	21
Specific Power, We/kg	5.1	2.8	8
Specific Power w/ATEGs We/kg	20.1	11.3	5.95

Howe Industries has conducted its own experiments to validate the RIC phenomena. Leveraging the (n, α) dopant materials, that are more readily available than radioisotopes, Howe Industries conducted a test on Boron Nitride (BN) at the Kansas State University, Mark II, TRIGA Reactor. A strong relationship in between the reactor power and the overall resistance of the BN sample is shown in Figure 4. A decrease, of up to 22 times, in resistance was recorded, while a nearly a 50 times decrease was observed by the reactor operations team (data recording equipment had a safety time out function, resulting in final two points being manually recorded). This experiment eludes to the possibility of (n, α) RIC dopants through ^{10}B dopants is feasible. BN while not suitable for ATEGs in its pure bulk form, has been studied for TEG applications in the form of quantum dots, thin films, and nanoribbons/tubes by Ref. 7 and 8 Reference 9 has shown that a ZT of 2.5 is possible with graphene/h-BN (hexagonal BN) superlattice monolayers. If the changes in conductivity observed from the KSU experiment hold true for BN in this superlattice, a *zT* potential of greater than 50 is theoretically possible (using only recorded values, and over 100 using the observed values) which corresponds to an efficiency of 33.4% (and 35.5% for the observed points) according to Eq. (3), using SPEAR's expected temperature gradient. This would far exceed any thermoelectric technologies currently available. In another study conducted by Reference 10, involving graphene-boron nitride hetero-structures of various widths, a ZT value of 0.9 was found to be theoretically possible. Again, if the same change in conductivity is observed as in the BN experiment, this would result in a ZT value 19.8, corresponding to a 28.8% efficiency (32.7% from observed points).

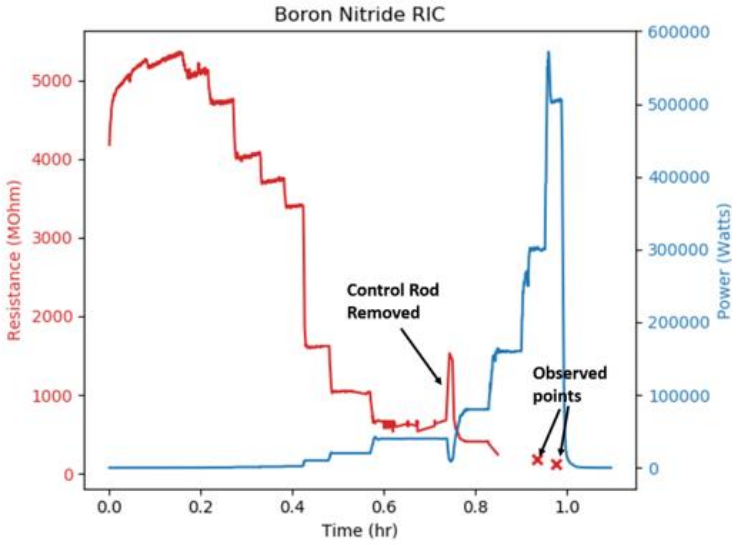

Figure 4. Boron Nitride results from experiments in a Trigga Mark II reactor. A strong association is visible between the reactor power and material resistance. Reactor operator observed data points after recording capabilities on experimental equipment timed out.

III. Nano-Reactor System

On top of the SPEAR probe rests a 15kWt nuclear reactor. The ATEG power conversion system is expected to operate at a conservative 20% efficiency to extract 3kW of electrical power. This compact reactor has a mass less than 150kg and could be commercially available to private companies within the United States. An artist rendering of the reactor is visible in Figure 5.

Low-Enriched Uranium (LEU) consists of <20% enriched ^{235}U, with the remainder being ^{238}U.[11] Whereas, Highly Enriched Uranium (HEU) contains a higher atomic density of ^{235}U, which allows for a greater fraction of neutrons to cause fission, and therefore allowing for a smaller volume/mass of uranium to reach criticality[12]. While this may help to produce a smaller reactor, the proliferation

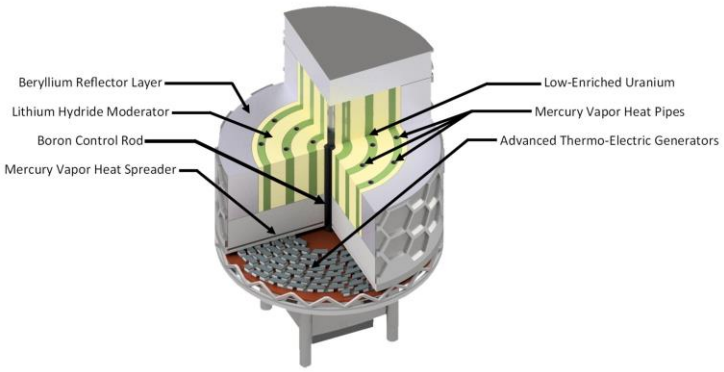

Figure 5. SPEAR's nano-reactor with its various components enabling the criticality of the low enriched uranium fuel to produce 15 kW of thermal power. The ATEG power conversion system harvests approximately 3 kW of electrical power and are located at the base of the reactor to ensure exposure to the neutron field. Total reactor mass is under 150 kg.

of HEU is a primary concern for the US government and other national governments, making it significantly more difficult for private companies to work with. According to Ref. 13, "The use of LEU is consistent with US policy for civilian fission systems, reduces security-related costs and schedule impacts (compared to HEU), and greatly increases programmatic flexibility to allow extensive participation by industry and academia".

Although HEU reactors may reduce launch costs, due to lower reactor masses, it is likely that a specialized, and larger, standby force would be needed for an HEU launch for recovery efforts to prevent HEU from falling into the wrong hands, in case of an accident[12]. While the government may have the ability to launch HEU reactors at lower costs, commercial entities will most likely by restricted to only LEU, as it will be much cheaper to handle. The uranium within the SPEAR nano-reactor will be enriched to 19.75% to remain classified as LEU and avoid security and regulatory issues. Producing only 15 kWt of power also reduces the size of the reactor, whereas most NEP reactors are designed in the multi-megawatt power range, increasing launch costs and reactor complexity.

.

When combined with an appropriate moderator and encased in a reflector, LEU is perfectly suitable for energy generation on the scale suitable for a spacecraft the size of SPEAR, and with limited mass penalties. LiH was selected as the moderator due to its high hydrogen density. Hydrogen atoms are the most efficient particles for slowing down fast neutrons, due to their similar masses[13]. Utilizing LiH increases the amount of hydrogen, but reduces the operating temperature from 4000K[15] for graphite, down to 961K[16] for LiH. Although, this may hinder designs utilizing current TEG technologies, the highly efficient ATEGs are able to extract large amounts of electrical power from the reactor. Resting on a heat spreader plate, the hot side of the ATEGs is maintained at 600K using mercury heat pipes. The cold side of the ATEGs connect to a heat pipe, which dissipates the 12kW of thermal energy, from the reactor, using four large radiators. The ATEGs have been located as close as possible to the reactor to remain within its neutron flux. While the ATEGs utilizing radioisotope RIC dopant particles would contain their own source of ionizing radiation, eliminating the need for a neutron field. However, due to the uncertain availability of suitable radioisotope particles, SPEAR has been designed in such a manner to promote the use of (n, α) ATEGs.

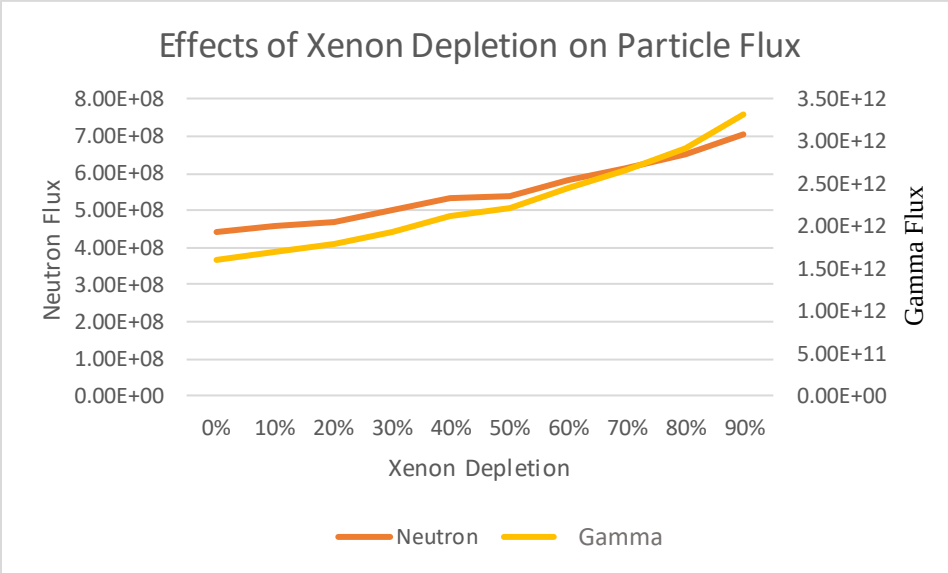

Figure 6. Neutron and gamma flux effected by the amount of xenon depletion. This flux represents the number of neutrons that have traveled through the propellant tanks to the front of the shield.

Radiation from the nuclear reactor is a primary concern for the CubeSat payload and onboard computers. SPEAR's shadow shield has been designed to protect the vital areas of the spacecraft from the harmful radiation that the reactor produces. The shield takes the shape of a cross to match the orientation of the CubeSat dispensers. The neutron shield itself is made from tetramethylammonium borohydride (TMAB $C_4H_{16}NB$); which is a relatively light weight material and is extremely effective for shielding in nuclear system. The hydrogen density within TMAB allows it to thermalize neutrons, and since the boron inherently has a large thermal neutron capture cross section, absorbs neutrons coming from the reactor.

Aiding in the protection of the CubeSats are the large tanks of xenon placed in front of the shield. Each propellant tank contains compressed xenon, and with this added mass between the CubeSats and the reactor, the total dose observed decreases. Throughout the mission however, the mass of propellant will decrease, increasing the effective dose rate to the payload. A study was conducted to better understand how the neutron and gamma flux will change with varying masses of xenon to simulate a journey to Europa. These results displayed in Figure 6, show there is an observable decrease in both neutron and gamma flux as the mass of the shield is increased. Also, the addition of the propellant tanks aids in slowing down the neutrons and gammas before striking the shield.

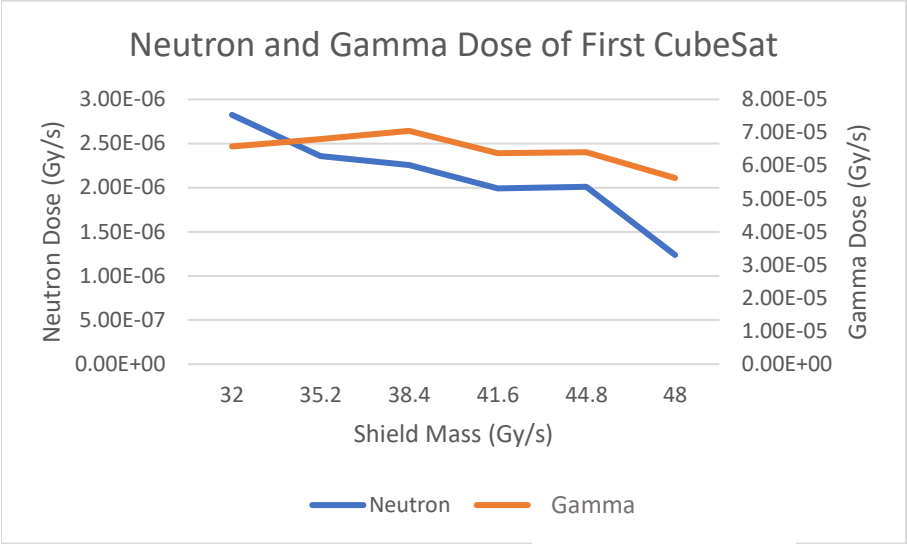

Figure 7. Neutron and gamma dose rate for a CubeSat positioned directly behind the shield. In reality there would be space between the shield and CubeSats filled with reaction wheels, electronics, deployment mechanisms, and individual shielding for the CubeSats in the Europa environment.

The shield's current mass is 32 kg, which results in a dose of 0.274 mGy/s directly behind the shield. A study was conducted to determine the dose a CubeSat positioned directly behind the shield would be exposed to, as a worst-case scenario. In order to decrease the CubeSat's exposure, the shield thickness was increased. This is represented as a total mass increase of the shield. These results are shown in Figure 7. Increasing the thickness/mass of the shield allowed for a greater portion of neutrons and gamma rays to be blocked, resulting in a slightly smaller dose. It should be noted, the CubeSats are arranged linearly, resulting in the CubeSat closest to the reactor having the highest dose.

There are several methods which can be used to limit the radiation dose the CubeSats receive even further. The first method is to limit the amount of time the reactor is critical; the reactor can be ramped down while waiting for phase change maneuvers to be completed, reducing exposure to the shield and CubeSats. Secondly, by increasing the shield thickness/mass will aid in the reduction of dosage as was observed in Figure 8. Thirdly, by organizing the payload in another fashion may also achieve a greater reduction in dosage, while maintaining the same shield mass. If all CubeSats can be placed in a linear fashion, a greater majority of the shield's mass can be placed in front of the CubeSats. Lastly, by increasing the distance between the reactor and the shield can also be an effective method to reduce the total dose absorbed. At ~3m from the reactor, the total dose for all four CubeSats directly behind the shield was 0.276 mGy/s; when the distance was increased to 6 meters, the total dose was decreased to 0.0889 mGy/s. Current radiation hardened components for CubeSats will need improvement to survive this dose rate for the duration of the mission, change to the shield geometry and mass will also be considered.

IV. Radiator Design

Four large radiators surround the SPEAR probe enables the system it to reject up to 12 kW of thermal power. These radiators will need to reject this amount of heat in various environments during its journey to Europa. The surface area required as a function of fins and surface properties was first considered. To provide an analytical relation for the radiator's performance, steady-state and isothermal assumptions were invoked. Additionally, a simple view factor, F_{self}, for self-radiation was considered as a function of n_{fins}, number of radiator panels (or "fins") arranged about the central pylon. Considering a combined value for solar and planetary heat sources, the required area of the isothermal radiator to get rid of the heat load, $Q_{th,w}$ = 12 kW_{th}, can be written,

$$A = \frac{Q_{th,w}}{n_{fins}\{2\,\epsilon_T \sigma (T^4 - T_\infty^4)(1 - F_{self})\} - \sum n_{facing}\alpha_{obj}\, I_{obj}} \quad (4)$$

where,

$$F_{self} = 1 - \sin\left(\frac{\pi}{n_{fins}}\right) \quad (5)$$

Equation (5) is the 2D version of the view factor for plates arranged like the radiators. This was used in the initial estimate to follow the theme of conservatism. This value is larger than the associated 3D version of F_{self}. For example, at 90° separation, the two panels in 3D are, $F_{self,3D}$ = 0.20004 while $F_{self,2D}$ = 0.2930. The solar constant, I_{sol} = 1.367 kW/m^2, is the magnitude of the solar irradiation at the distance between the Earth and the Sun[17]. The design variables included in Eq. (4), for a specified load of $Q_{th,w}$, are the n_{fins}, the equilibrium temperature, T, and the surface optical properties of absorptivity, α, an emissivity, ϵ. The surface property values can differ between the solar spectrum and strictly infrared sources. Using Eqs. (4) & (5), the required area for a single side of one radiator panel is plotted for various levels of solar absorptivity, over a range of n_{fins}, in Fig. 8.

For the radiators, low absorptivity in the solar spectrum is desired in order to decrease the external heat loads added to the material. On the other hand, the main purpose of the radiator is to radiate as much energy as possible. Therefore, having high emissivity in the infrared (IR) range is especially important. For these reasons, each radiator was assumed to use a white paint containing of magnesium oxide and aluminum oxide which provides the desired optical properties for the surface.

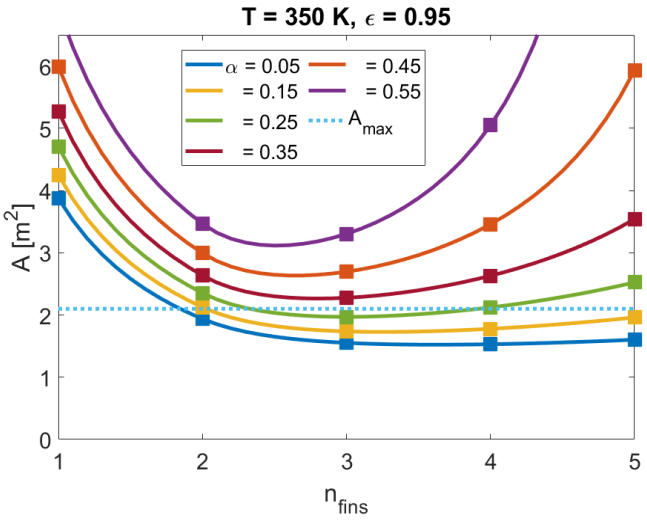

Figure 8. Radiator panel area (single face) to reject $Q_{th,w}$/ n_{fins} of heat while experiencing heat sources from the space environment.

Both the material selection and wall design of the radiators dictate to the extent which they approach the goal of an isothermal surface. Transient multphysics simulations were run to evaluate the actual temperature distribution, and thus performance as a radiator. Table 2 provides results from four such simulations, showing it takes four radiator panels (n_{fins} = 4) to handle the heat load, while maintaining temperatures near or below the design temperature of 350K, as shown for Fig. 8. Note that the hollow copper and pyrolytic graphite design is the only one to achieve under 50 kg while all designs were able to sufficiently radiate the needed heat load.

Table 2: Single radiator performance results with ideal surface properties (n_{fins} = 4)

Design Case	T_{mean} , T_{max} [K]	Max ΔT [K/s]	Mass [kg]	Specific Mass [kg/kW]
A1 (Solid: Al)	350, 357	5.5	79	25
A2 (Solid: Cu, PG)	345, 351	6.3	92	33
B1 (Solid: Cu, PG)	346, 351	6.6	79	25
B2 (Hollow: Cu, PG)	346, 351	8.1	28	9

The SPEAR probe thermal environment was also considered along its trajectory to Europa. While heat generation from the reactor is much higher than those from environmental sources, there is still the need to understand the thermal response of the vehicle throughout an extended journey through space; as isolated areas, far from the reactor, and out the Suns view, could get dangerously cold. Performing a thermal analysis of the full vehicle helps identify these problem areas so proper thermal management techniques can be applied. Such techniques could include thermal straps, additional heat pipes to transfer heat to an isolated component or add an electric or radioisotope heater. The severity and duration of a cold or dangerously hot spot, will dictate what thermal management strategy is applied.

Figure 9 (top) shows the trajectory of the SPEAR vehicle in terms of range from the Sun, Earth and Jupiter. The first two ranges are normalized by one astronomical unit (1 AU = 149.6 million kilometers), which equals the distance from the Sun to the Earth. The range to Jupiter is normalized by the final orbit, making the curve end at Range = 1.

Unfortunately, only the final months of the overall trip were provided in the Jupiter reference frame, hence the short curve for $R_{jupiter}$. As can be seen from the corresponding heat flux attributed to each of these celestial bodies (Figure 9, bottom), the final approach heating from Jupiter is orders of magnitude lower than that from the Sun. Similarly, it should be noted that the trajectory's proximity to the orbit of Mars was not considered but would result in an additional heat source. This would be of similar magnitude to the heating of Earth, at a maximum, during closest approach. However, since Mars is not the destination, it is likely this source of heat will not be significant, and thus its exclusion from the current study is reasonable.

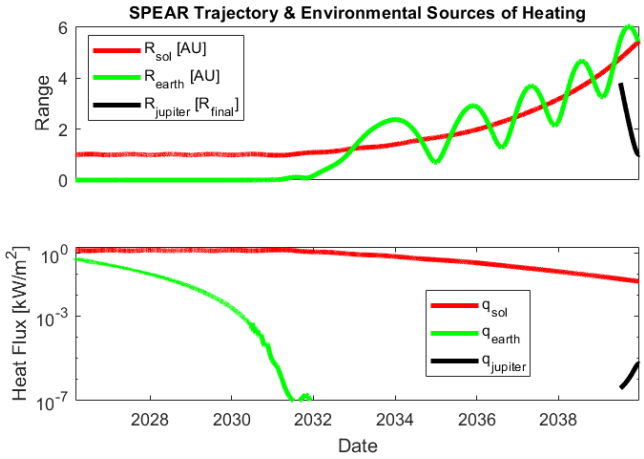

Figure 9. (*Top*) Trajectory data shown as nondimensional ranges from the Sun, Earth and Jupiter. (*Bottom*) Maximum heat fluxes expected from space environment. Shared x-axis (*at bottom*).

Figure 10 shows the full vehicle's temperature distribution as it reaches Jupiter. Cold regions (<200K) are shown in blue. The reactor, being isolated from this model, represents the temperature of the ATEG heat rejection. For the propellant tanks, this is desirable as the Xenon inside is intended to be at its triple point (~166 K). One of the tanks, which is in the direct sunlight, is noticeably warmer than the others. No rolling was considered in the trajectory and for a large portion, the sun remains facing a single side of the vehicle. Future work will need to consider the energy requirements of inducing a roll at a given rate, as needed to maintain more uniform temperature around the vehicle.

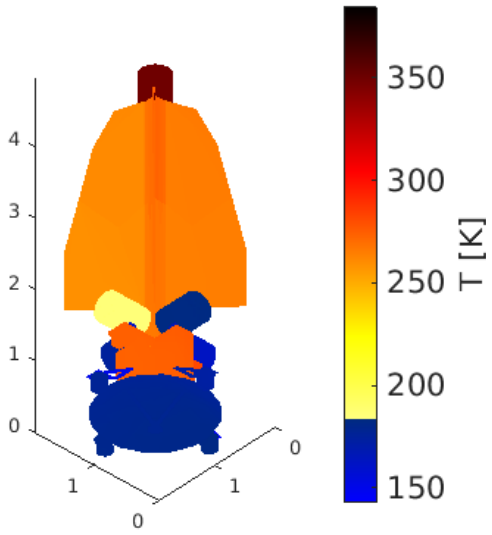

Figure 10. Thermal analysis results from the full mission trajectory. Note, worse case heating scenario considered where failure in roll control is exhibited.

Additional simplifications inherent to the current full vehicle model are a lack of internal heat sources from subsystems, such as: the power conditioning unit, communication electronics and electric thrusters. These sources are small in comparison to that of the waste heat of the reactor and to a lesser extent, the external heat sources from celestial bodies. However, as the full vehicle simulations show some of these portions of the vehicle are reaching very cold temperatures (<200K). Including these internal sources of heat will act to both increase the fidelity of these results and show increased viability in the expected temperature ranges for the proposed mission. If these internal sources do not suffice to ensure the temperature limits desired for the final mission plan, many design options exist to mitigate the problem. These include additional heat pipes to transfer heat to other parts of the vehicle, or local heaters if additional heat pipes are not desired.

V. Conclusion

Through the Phase I NIAC study, Howe Industries, and its partners, have shown the potential for success of the SPEAR probe. Its highly efficient ATEG power conversion system far outpaces any solid-state power production method currently available. The SPEAR probe could offer unparalleled access to deep space for commercial companies, government organizations, and universities to deliver high impact science payloads. It should be noted that while the SPEAR probe has been designed to deliver a swarm of CubeSats to Europa, it could be retrofitted to fit up to 70 kg of science payload with minimal design changes to the radiation shield and other sub-systems. The ATEG

power conversion system enabling the success of SPEAR, has far broader applications and could see use in other space-based power systems, as well as terrestrial based systems. A Phase II NIAC study would involve further testing of the ATEG power conversion system through several material sweeps. Howe Industries has already identified several potential materials that could be made into a working ATEG prototype for testing within a nuclear reactor. The SPEAR probe design will see further refinement to its systems, most notably to the radiation shield, electrical power system, and radiator design. The Europa mission will also be expanded upon, with a full trajectory and mission operations for the SPEAR probe and its CubeSat swarm. The SPEAR system shows promise to develop and explore deep space economically and efficiently.

Acknowledgements

A special thanks to the Atomos Space team for assisting Howe Industries in this Phase I NIAC study. In addition, thank you to Dr. Alan Cebula from KSU for allowing us to use their reactor. Additional thanks to NIAC for providing the funding for this study.

References

[1]H. M. Salh, "Improving the Overall Efficiency of Radioisotope Thermoelectric Generators," *Advances in Energy and Power*, pp. 21-26, 2014.

[2]S. J. Zinkle and L. K. Mansur, "Radiation Effects in Materials, with Emphasis on INsulators for Couplers," Oak Ridge National Laboratory, 2002.

[3]T. Shikama, S. J. Zinkle and S. Yamamoto, "Electrical properties of ceramics during reactor irradiation," *Journal of Nuclear materials*, Vols. 258-263, pp. 1867-1872, 1998.

[4]M. Niffenegger and et. al., "The change of the Seebeck coefficient due to neutron irradiation and thermal fatigue of nuclear reactor pressure vessel steel and its application to the monitoring of material degradation," Paul Scherrer Institute , Switzerland, 2002.

[5]S. Zinkle and E. Hodgson, "Radiation-induced changes in the physical properties of ceramic materials," *Journal of Nuclear Materials* , Vols. 191-194, pp. 58-66.

[6]NASA, "Advanced Stirling Radioisotope Generator (ASRG)," NF-2013-07-568-HQ, 3 9 2013. [Online]. Available: https://rps.nasa.gov/system/downloadable_items/36_APP_ASRG_Fact_Sheet_v3_9-3-13.pdf.

[7]J. Nakamura and A. Akaishi, "Anomalous enhancement of Seebeck coefficients of the graphene/hexagonal boron nitride composites," *Japanese Journal of Applied PHysics*, vol. 55, no. 1102A9, pp. 1-9, 2016.

[8]L. A. Algharagholy, Q. Al-Galiby, H. A. Marhoon, H. Sadeghi, H. M. Abduljalil and C. J. Lambert, "Tuning thermoelectric properties of graphene/boron nitride heterostructures," *Nanotechnology*, vol. 26, 2015.

[9]Z. Zhou, H. Liu, D. Fan and G. Cao, "Designing graphene/hexagonal boron nitride superlattice monolayer with high thermoelectric performance," 2019.

[10]L. A. Algharagholy et. al., "Tuning thermoelectric properties of graphene/boron nitride heterostructures," *Nanotechnology*, vol. 26, no. 47, 2015.

[11]Department of Energy, "Nuclear Materials Control and Accountability," *DOE Standard DOE-STD-1194-2011*.

[12]D. I. Poston and P. R. Mcclure, "White Paper-Use of LEU for a Space Reactor," Los Alamos National Laboratory, 2017.

[13]Marshall Space Flight Center, "Space Technology Game Changing Development Nuclear Thermal Propulsion (NTP)," NASA.

[14]P. M. Huerta, "A review of the cold neutron moderator materials: neutronic performance and radiation effects," *Physics Procedia*, vol. 60, no. 74-82.

[15]MatWeb, "Graphite, Carbon, C," 3 11 2016. URL: http://matweb.com/search/DataSheet.aspx?MatGUID=3f64b985402445c0a5af911135909344&ckck=1.

[16]MatWeb, "Lithium Hydride, LiH," 3 11 2016.. URL: http://matweb.com/search/DataSheet.aspx?MatGUID=b0f308c749af4598b3c776a75c4afe75.

[17]S. L. Rickman, "Introduction to On-Orbit Thermal Enviornments," in *THermal and Fluids Analysis Workshop*, Cleveland, Ohio, 2014.